Materials Today Bio 32 (2025) 101717

Contents lists available at ScienceDirect

Materials Today Bio

journal homepage: www.journals.elsevier.com/materials-today-bio

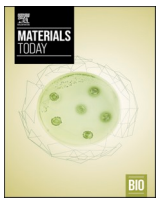

Renal-clearable and mitochondria-targeted metal-engineered carbon dot nanozymes for regulating mitochondrial oxidative stress in acute kidney injury

Jiangpeng Pan [a,b,1], Juntao Wang [c,1], Wei Wang [d,e,1], Ziyang Liu [b], Shuai Huo [a], Lei Yan [b], Wei Jiang [a,*], Fengmin Shao [a,b,**], Yue Gu [a,b,***]

[a] Department of Nephrology, Fuwai Central China Cardiovascular Hospital, Zhengzhou, Henan, 450003, China
[b] Department of Nephrology, Henan Clinical Medical Research Center for Nephropathy, Henan Provincial Key Laboratory of Kidney Disease and Immunology, Henan Provincial People's Hospital; Zhengzhou University People's Hospital; Henan University People's Hospital, Zhengzhou, Henan, 450003, China
[c] Department of Nephrology, The First People's Hospital of Shangqiu, Shangqiu, Henan, China
[d] Nanozyme Laboratory in Zhongyuan, School of Basic Medical Sciences, Zhengzhou University, Zhengzhou, 450001, China
[e] Nanozyme Laboratory in Zhongyuan, Henan Academy of Innovations in Medical Science, Zhengzhou, Henan, 451163, China

ARTICLE INFO

Keywords:
Acute kidney injury
Carbon dots nanozymes
Renal-clearable
Mitochondria-targeted
Antioxidant

ABSTRACT

Mitochondrial dysfunction-induced oxidative stress is a key pathogenic factor in acute kidney injury (AKI). Despite this, current mitochondrial-targeted antioxidant therapies have shown limited efficacy in clinical settings. In this study, we introduce a novel renal-clearable and mitochondria-targeted antioxidant nanozyme (TPP@RuCDzyme) designed to precisely modulate mitochondrial oxidative stress and mitigate AKI progression. TPP@RuCDzyme was synthesized by integrating ruthenium-doped carbon dots (CDs) with triphenylphosphine (TPP), a mitochondria-targeting moiety. This nanozyme system exhibits cascade enzyme-like activities, mimicking superoxide dismutase (SOD) and catalase (CAT), to efficiently convert cytotoxic superoxide ($O_2^{\bullet-}$) and hydrogen peroxide (H_2O_2) into non-toxic water (H_2O) and oxygen (O_2). This dual-enzyme mimicry effectively alleviates mitochondrial oxidative damage, restores mitochondrial function, and inhibits apoptosis. Compared to RuCDzyme alone, TPP@RuCDzyme demonstrated significantly enhanced efficacy in alleviating glycerol-induced AKI by inhibiting oxidative stress. By leveraging the catalytic activity derived from the integration of CDs and a metallic element, this study presents a promising therapeutic strategy for AKI and other renal diseases associated with mitochondrial dysfunction.

1. Introduction

Acute kidney injury (AKI) is a common and severe clinical syndrome with a high incidence rate, high mortality rate and high medical expenses and has thus become a significant health concern [1,2]. The fundamental clinical diagnostic criterion for AKI is an increase in serum creatinine (CRE) levels by 50% within one week, or by more than 26.5 μmol/L every 48 h [3,4]. Each year, approximately 13.3 million individuals develop AKI, with 1.7 million succumbing to the condition [4,5]. AKI is an independent risk factor for mortality among patients in the emergency department, and 30 %–70% of AKI cases progress to chronic kidney disease or end-stage renal disease [6]. Reactive oxygen species (ROS) react with lipids, nucleic acids and proteins, leading to oxidative stress and inflammation, and are closely associated with AKI under several circumstances, thereby causing renal toxicity [7,8]. Clinically, besides supportive treatment and renal replacement therapy, there is no specific medication for ameliorating AKI [3,9].

The main pathological manifestation of AKI is the outburst of ROS, which causes severe damage to renal cells, particularly proximal tubular cells [10]. In the AKI process, once renal cells are impaired, a large quantity of ROS is generated. The major source of ROS is the mitochondria, whose electron transport chain is prone to interference by

* Corresponding author. Department of Nephrology, Fuwai Central China Cardiovascular Hospital, Zhengzhou, Henan, 450003, China.
** Corresponding author. Department of Nephrology, Fuwai Central China Cardiovascular Hospital, Zhengzhou, Henan, 450003, China.
*** Corresponding author. Department of Nephrology, Fuwai Central China Cardiovascular Hospital, Zhengzhou, Henan, 450003, China.
E-mail addresses: weijiang@zzu.edu.cn (W. Jiang), fengminshao@126.com (F. Shao), guyuesunny@zzu.edu.cn (Y. Gu).
[1] J.P., J.W., and W.W. contributed equally to this work.

https://doi.org/10.1016/j.mtbio.2025.101717
Received 9 January 2025; Received in revised form 10 March 2025; Accepted 28 March 2025
Available online 28 March 2025

various factors, resulting in ROS production [11,12]. These ROS not only directly harm renal cells but also trigger a series of inflammatory and oxidative stress responses, further worsening renal injury [13,14]. Simultaneously, ROS influences the energy metabolism and mitochondrial function of renal cells, leading to cell death and renal function deterioration [14–16]. To maintain redox equilibrium, renal cells rely on endogenous antioxidants, such as catalase (CAT), Superoxide dismutase (SOD) and glutathione (GSH), for ROS scavenging [17,18]. Nevertheless, during the AKI process, the scavenging capacity of endogenous antioxidants is often insufficient to deal with the massive ROS amounts. Hence, developing new drugs or therapeutic approaches that can target mitochondria and alleviate mitochondrial oxidative stress is important for AKI treatment. Recent research has discovered that some nanomaterials [19–22], possess excellent antioxidant and ROS scavenging abilities, offering novel ideas for AKI treatment.

Nanozymes, which are organic or inorganic nanomaterials with inherent enzymatic properties [23,24], have demonstrated remarkable efficacy in ROS antioxidation and scavenging [25,26]. By mimicking the catalytic activity of natural enzymes, nanozymes can regulate the redox balance within organisms, thereby exerting antioxidant functions [26,27]. They can catalyze ROS decomposition, reduce oxidative stress levels and protect cells from oxidative damage. Nanozymes catalyze the decomposition reactions of ROS, such as decomposition of hydrogen peroxide (H_2O_2) into water and oxygen (O_2) and conversion of superoxide anion radicals ($O_2^{\bullet-}$) into H_2O_2 and O_2 [28–30]. These reactions lower the ROS concentration, thereby alleviating the damage to cells caused by oxidative stress. Nanozymes can also exert antioxidant effects by regulating the redox balance within organisms [31]. Various nanozymes have been designed to protect against oxidative damage [32,33].

Carbon dots (CDs), as a novel type of carbon-based nanomaterial, exhibit remarkable potential in biomedical applications due to their small particle size [34–36], excellent biocompatibility [37,38], and ease of modification [39–41]. Moreover, CD nanozymes have gradually attracted attention in recent years [42–44].

Ru-based nanozymes are utilized for the treatment of various diseases owing to their multiple enzyme-like activities. Zhou Liu et al. reported the synthesis of RuO_2 nanozymes with excellent biocompatibility and enzyme-like activities, which demonstrated remarkable cellular protection against renal toxicity caused by oxidative stress [45]. Wu et al. reported a RuO_2-PVP nanozyme as a single-component and multienzyme-mimicking nanoplatform for ROS scavenging. The fabricated RuO_2-PVP nanozyme demonstrated a significant protective effect on redox homeostasis and had outstanding ROS elimination capabilities against inflammation and Parkinson's disease *in vitro* and *in vivo* [46].

In this study, CDs were synthesized using the hydrothermal method and combined with Ru to construct RuCDzyme nanoparticles. Moreover, through modification based on triphenylphosphine (TPP), RuCDzyme was endowed with mitochondrial targeting capability (Scheme 1). This nanocomposite can serve as an outstanding antioxidant nanozyme to safeguard the biological system from ROS-induced damage. The synthesized TPP@RuCDzyme demonstrates highly efficient cascade catalytic activity. It not only functions as a SOD mimic to catalyze the decomposition of superoxide radicals ($O_2^{\bullet-}$) into hydrogen peroxide (H_2O_2), but also mimics catalase to further catalyze H_2O_2 into water (H_2O) and oxygen (O_2). TPP@RuCDzyme can also significantly scavenge other free radicals, such as 2, 2′-azinobis-(3-ethylbenzthiazoline-6-sulphonate) (ABTS) and 2,2-diphenyl-1-picrylhydrazyl (DPPH). The TPP@RuCDzyme can scavenge various ROS *in vivo* and *in vitro*, thereby effectively exerting a therapeutic effect on rhabdomyolysis-induced AKI.

2. Experimental section

2.1. Chemicals and materials

Folic acid, Glutathione, Formamide, Ruthenium (III) chloride hydrate ($RuCl_3{\cdot}xH_2O$), 3-Carboxypropyltriphenylphosphonium bromide

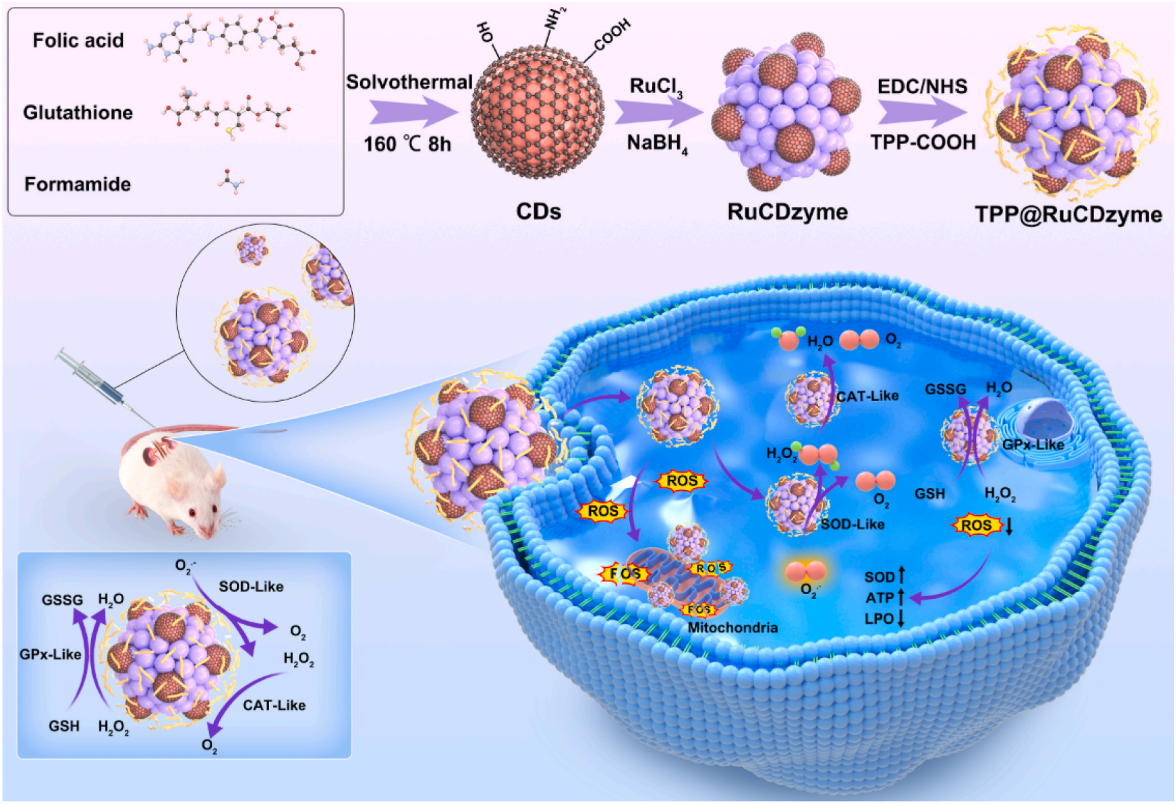

Scheme 1. Schematic diagram illustrating the preparation process of TPP@RuCDzyme and TPP@RuCDzyme as antioxidants to alleviate AKI through removing excessive ROS.

(TPP-COOH), N1-((Ethylimino)methylene)-N3 (EDC), 1-Hydroxypyrrolidine-2,5-dione (NHS) were purchased from Aladdin Reagent (China). Cytochrome C (CytC), Hydrogen peroxide (H_2O_2, 30%), DPPH, ABTS, and 2',7'-Dichlorodihydrofluorescein diacetate (DCFH-DA) were bought from Sigma-Aldrich (USA). Reactive Oxygen Species Assay Kit, Apoptosis Detection kit (propidium iodide/annexin V-FITC) were obtained from Beyotime Institute of Biotechnology (China). The lipid hydroperoxide (LPO), SOD, and ATP Test Kits were purchased from Beijing Solarbio Technology Co., Ltd. The CRE and blood urea nitrogen (BUN) assay kits were procured from Nanjing Jiancheng Bioengineering Research Institute. The ELISA kits for Kidney injury molecule 1 (Kim-1), Heme oxygenase 1 (HO-1), and 8-hydroxy-2'-deoxyguanosine (8-OHdG) were procured from Shanghai Enzyme-Linked Immunosorbent Assay Biotechnology Co., Ltd. All the aqueous solutions were prepared using purified deionized (DI) water purified with a purification system (Direct-Q3, Millipore, United States).

2.2. Synthesis of CDs

2.1 g of glutathione and 0.105 g of folic acid were dissolved in 70 mL of formamide. The solution was then transferred to an autoclave and reacted at a temperature range of 140–160°C for 6–12 h. After the reaction, the mixture was centrifuged at 3000 rpm for 10 min to remove the precipitate. The supernatant was subsequently dialyzed for 5–7 days using a dialysis bag with a molecular weight cut-off of 3500 Da. Finally, the dialyzed solution was ultra-filtered using Millipore centrifuge filter devices equipped with 100 kDa MWCO membranes. The fractions with a molecular weight less than 100 kDa were collected.

2.3. Synthesis of RuCDzyme

The pH of the CDs solution (0.5 mg/mL, 1.6 mL) and ruthenium (III) chloride hydrate solution (10 mM, 0.4 mL) was adjusted to alkaline by adding 800 μL of 0.5 M NaOH under stirring. Following the dropwise addition of 3 mL of 10 mg/mL $NaBH_4$ solution, the mixture was stirred for 3 h at room temperature and then left to stand overnight. The resulting solution was neutralized with hydrochloric acid and subsequently dialyzed for 3 days.

2.4. Synthesis of TPP@RuCDzyme

2 mg of TPP-COOH were accurately weighed and dissolved in deionized water. EDC and NHS were subsequently added, and the mixture was stirred at room temperature for 0.5 h to activate TPP-COOH. The molar ratio of TPP-COOH, EDC, and NHS was maintained at 1:1:1.2. Following this, 40 mg of RuCDzyme was introduced, and the solution was stirred continuously at room temperature for an additional 24 h. Upon completion of the reaction, dialysis was performed for 24 h using a dialysis membrane with a molecular weight cutoff of 8000–14000 Da. Finally, the TPP@RuCDzyme was obtained via vacuum freeze-drying.

2.5. Catalase-like activity of RuCDzyme and TPP@RuCDzyme

To investigate the catalase-like activity of RuCDzyme and TPP@RuCDzyme, 200 μL of 100 mM H_2O_2 and 200 μL of RuCDzyme or TPP@RuCDzyme solution were added to 10 mL of 0.01 M buffer solution at 25°C. The change in dissolved oxygen content in the system was immediately measured using a dissolved oxygen meter after vortex mixing.

2.6. SOD-like activity of RuCDzyme and TPP@RuCDzyme

The SOD-like activity of RuCDzyme and TPP@RuCDzyme was determined using the xanthine oxidase method. Briefly, 30 μL of prepared nanozyme solutions were transferred into a 96-well plate. Xanthine, pH 7.4 phosphate buffer, Cytochrome C and xanthine oxidase working solution were added sequentially. The absorbance of each well at 450 nm was immediately measured before and after a 1-min interval using a microplate reader. Each group was assayed in triplicate.

2.7. GPx-like activity of TPP@RuCDzyme

In accordance with the manufacturer's instructions, GPx-like activity was assessed using the GPx activity assay kit (Solarbio) based on the coupled reductase method. Specifically, varying concentrations of TPP@RuCDzyme (0–1 mg/mL) were employed to evaluate GPx-like activity. GPx catalyzes the oxidation of GSH by H_2O_2 to form GSSG. The reduced GSH reacts with DTNB to produce a compound that exhibits a characteristic absorption peak at 412 nm. The decrease in absorbance at 412 nm directly reflects the enzymatic activity of GPx.

2.8. ABTS radical-scavenging activity of RuCDzyme and TPP@RuCDzyme

The ABTS radical cation discoloration test was utilized to measure the free radical scavenging capacity of the prepared nanozymes. First, ABTS radical cations ($ABTS^+$) were generated by mixing 7 mM ABTS aqueous solution with 2.45 mM potassium persulfate and incubating for 16 h. Next, different concentrations of RuCDzyme and TPP@RuCDzyme (0–200 μg/mL) were added to the above mixture. Finally, the absorbance at 734 nm of the resulting solutions was measured using a spectrophotometer, and the scavenging efficiency of ABTS was calculated as follows:

$$\text{ABTS radical cations scavenging activity} = [1-(A_i-A_1)]/A_0 \times 100\%.$$

A_0 is the absorbance of ABTS solutions without adding samples; A_i is the absorbance of the sample after reacting with ABTS; A_1 is the absorbance of solvent mixed with nanozymes.

2.9. DPPH radical cations scavenging activity of RuCDzyme and TPP@RuCDzyme

Different concentrations of RuCDzyme and TPP@RuCDzyme were prepared and mixed with DPPH (125 μM) in equal volumes of ethanol. The final concentrations of RuCDzyme and TPP@RuCDzyme ranged from 0 to 200 μg/mL, while the final DPPH concentration was 62.5 μM. After a 30 min reaction period, the absorbance of DPPH at 517 nm was measured. The scavenging efficiency of DPPH was calculated using the following equation:

$$\text{DPPH radical cations scavenging activity} = [1-(A_i-A_1)]/A_0 \times 100\%.$$

A_0 is the absorbance of DPPH solutions without adding samples; A_i is the absorbance of the sample after reacting with DPPH solutions; A_1 is the absorbance of solvent mixed with nanozymes.

2.10. Cell culture

Human kidney-2 (HK-2) cells were obtained from the American Type Culture Collection (ATCC) and cultured in Dulbecco's Modified Eagle Medium (DMEM) supplemented with 1% penicillin/streptomycin and 10% fetal bovine serum (FBS). Cells were maintained at 37°C in a humidified atmosphere containing 5% CO_2.

2.11. Cell cytotoxicity

HK-2 cells were seeded at a density of 8000 cells per well in a 96-well plate and incubated for 24 h. Subsequently, the cells were treated with varying concentrations of TPP@RuCDzyme (0–200 μg/mL). After treatment periods of 24 and 48 h, cell viability was assessed using the Cell Counting Kit-8 assay.

2.12. Hemolysis assays

Red blood cells were isolated from serum by centrifugation at 1500 rpm for 10 min. The cells were then incubated with different concentrations of RuCDzyme and TPP@RuCDzyme (25–400 μg/mL) in PBS at 37°C for 30 min. Following incubation, the mixture was centrifuged again, and 100 μL of the supernatant was collected to measure its absorbance at 578 nm using a microplate reader.

$$\text{Hemolysis ratio} = [OD_{(sample)}\text{-}OD_{(PBS)}]/[OD_{(ddH2O)}\text{-}OD_{(PBS)}] \times 100\%$$

2.13. Protection of cells with H_2O_2 stimulation by RuCDzyme and TPP@RuCDzyme

HK-2 cells were seeded in a 96-well plate at a density of 8000 cells per well and incubated for 24 h. Subsequently, the cells were treated with RuCDzyme and TPP@RuCDzyme at various concentrations (0–200 μg/mL) for 2 h. Next, the cells were exposed to 400 μM H_2O_2 for 24 h in the dark. Finally, cell viability was assessed using the CCK-8 assay.

HK-2 cells were seeded in six-well plates at a density of 15,000 cells per well and incubated for 24 h. Subsequently, the cells were treated with RuCDzyme and TPP@RuCDzyme at a concentration of 50 μg/mL for 2 h. Next, the cells were exposed to 400 μM H_2O_2 for 24 h in the dark. Finally, cell viability was assessed using 1 μM Calcein AM (for live cells) and 2 μM propidium iodide (PI, for dead cells). Fluorescence images were captured using an inverted fluorescence microscope.

In addition, the apoptosis of HK-2 cells was evaluated using the Annexin V Apoptosis Detection Kit. Cells were treated and collected following the same protocol, then washed three times with cold PBS and stained with Annexin V and propidium iodide (PI). Finally, the stained cells were analyzed by flow cytometry.

2.14. Detection of intracellular ROS

Intracellular ROS levels were measured using 2′,7′-dichlorofluorescein diacetate (DCFH-DA) staining. HK-2 cells were seeded in six-well plates at a density of 15,000 cells per well and incubated for 24 h. Subsequently, the cells were treated with RuCDzyme and TPP@RuCDzyme at a concentration of 50 μg/mL for 24 h. The cells were then washed with PBS to remove unbound RuCDzyme and TPP@RuCDzyme. Next, the cells were exposed to 1 mM H_2O_2 for 30 min. Fluorescence images were captured using an inverted fluorescence microscope (emission wavelength: 520 ± 20 nm, excitation wavelength: 488 nm). Additionally, the cells were stained with DCFH-DA, incubated at 37°C for 30 min, and washed three times with PBS before being analyzed by flow cytometry.

2.15. AKI mouse model

The female Balb/c mice (6–8 weeks old, 17–21 g) used in this study were obtained from the Experimental Animal Center of Zhengzhou University. All animal experiments were conducted in accordance with protocols approved by the Animal Ethics Committee of the Experimental Animal Center of Zhengzhou University (ZZU-LAC20240419[01]).

Glycerol-induced AKI mouse model: Female Balb/c mice were dehydrated for 15 h but had free access to food. Subsequently, 50% glycerol was injected intramuscularly into both hind limbs at a dose of 8 mL/kg. Two hours post-injection, the AKI mouse model was successfully established and used for subsequent experiments.

2.16. Therapeutic effect in AKI mice

To analyze the therapeutic effects of RuCDzyme and TPP@RuCDzyme, we randomly divided the mice into four groups: (i) healthy mice treated with PBS; (ii) AKI mice treated with PBS; (iii) AKI mice treated with RuCDzyme; and (iv) AKI mice treated with TPP@RuCDzyme. After treatment, kidney function and body weight were monitored.

2.17. Kidney function evaluation

Twenty-four hours after intravenous injection of RuCDzyme and TPP@RuCDzyme, the mice were euthanized, and kidney and blood samples were collected. The kidney tissues were sectioned and stained with hematoxylin and eosin (H&E), and the levels of blood urea nitrogen (BUN) and creatinine (CRE) in the blood samples were measured.

2.18. Detection of biomarkers

Kidneys from each group were stored at −80°C until analysis. Kidney homogenates were prepared according to the respective assay protocols. Superoxide dismutase (SOD) activity was assessed using an SOD assay kit (Solarbio, China). The expression levels of kidney injury molecule-1 (Kim-1) and heme oxygenase-1 (HO-1) were measured using Kim-1 and HO-1 ELISA kits (mmbio, China). DNA damage was evaluated using a DNA damage competition ELISA kit (mmbio, China).

2.19. Confocal imaging of superoxide production in kidneys

To assess superoxide production histologically, kidneys obtained from mice were cryosectioned at −20°C. Frozen kidney tissue sections were washed with PBS and stained with 1 mM dihydroethidium (DHE) for 30 min to detect superoxide formation. The stained sections were then mounted on glass slides and imaged using a confocal microscope.

2.20. In vivo toxicity assessment

TPP@RuCDzyme (20 mg/kg) and PBS were intravenously injected into two groups of mice (n = 5) twice weekly for 14 days. At the end of the treatment period, organ and blood samples were collected from both groups. H&E staining was performed on sections of the heart, liver, spleen, lungs, and kidneys, and blood parameters were measured. The relevant blood parameters included: alanine aminotransferase (ALT), aspartate aminotransferase (AST), creatinine (CRE), blood urea nitrogen (BUN), white blood cells (WBC), lymphocytes (LYM), monocytes (MON), red blood cells (RBC), hemoglobin (HGB), mean corpuscular hemoglobin (MCH), hematocrit (HCT), mean corpuscular volume (MCV), mean corpuscular hemoglobin concentration (MCHC), platelets (PLT), platelet distribution width (PDW), mean platelet volume (MPV), and red blood cell distribution width (RDW).

3. Results and discussion

3.1. Synthesis and characterization of RuCDzyme and TPP@RuCDzyme

Scheme 1 illustrates the synthesis of TPP@RuCDzyme and its catalytic mechanism, biological effects and therapeutic effects on AKI mice. In brief, CDs were initially fabricated by heating a solution containing GSH, folic acid and formamide. Transmission electron microscope (TEM) images of CDs showed single-dispersed nanoparticles with a relatively small size of 2–3 nm (Fig. 1A). Subsequently, Ru^{3+} was reduced using $NaBH_4$ to form RuCDzyme. Finally, TPP was conjugated with RuCDzyme through an amidation reaction to obtain mitochondria-targeted TPP@RuCDzyme. TEM images and dynamic light scattering revealed that the average diameters of the synthesized TPP@RuCDzyme was approximately 85.69 nm (Fig. 1B; Fig. S2). Additionally, in Fig. S1, uniformly distributed spherical nanoparticles with a diameter of approximately 2–3 nm can be observed on the surface of TPP@RuCDzyme. This morphology and size are consistent with the CDs images observed in Fig. 1A. As depicted in Fig. 1C, the zeta potentials of the synthesized CDs and RuCDzyme were −14.98 mV and −39.39 mV,

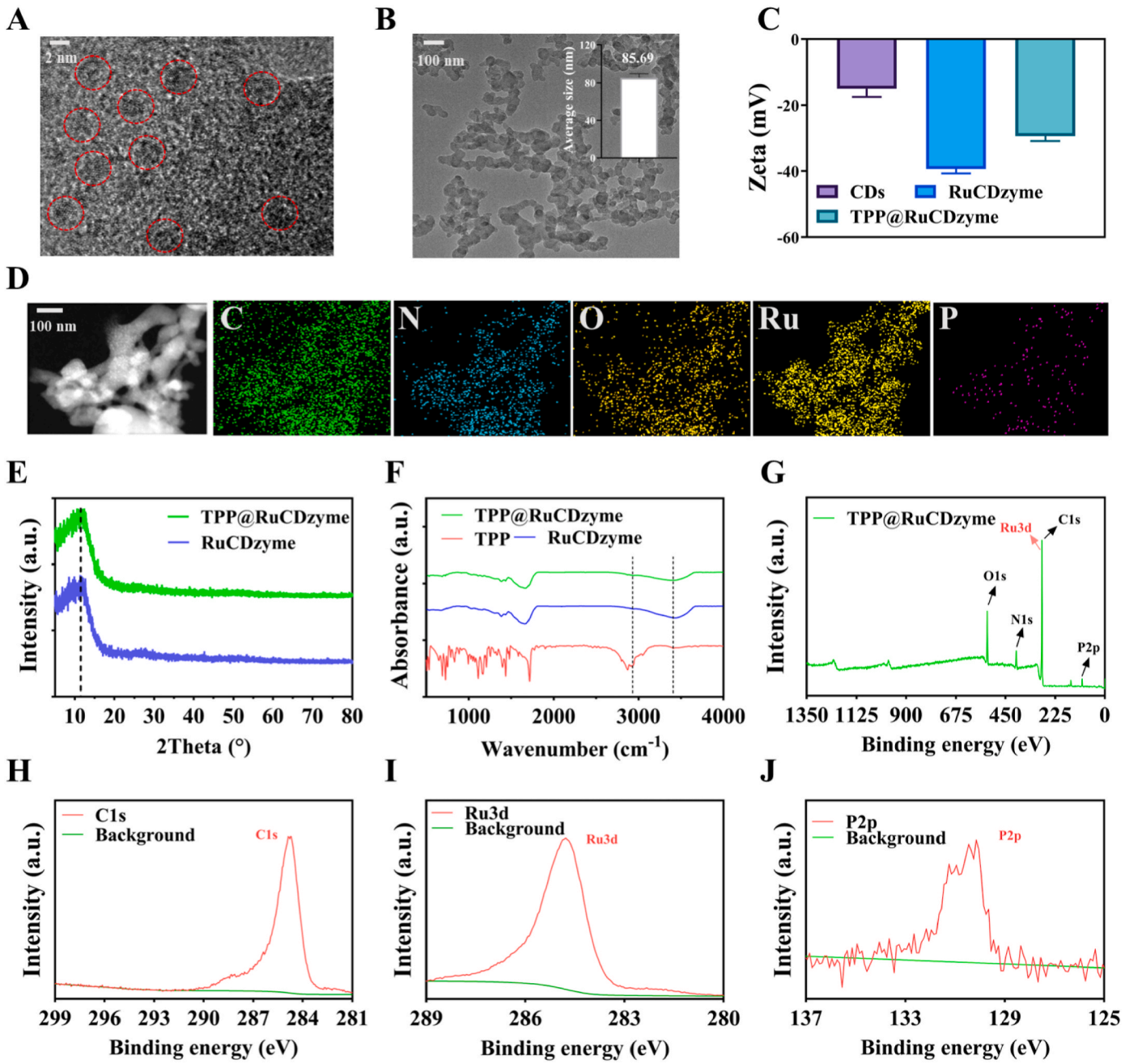

Fig. 1. Fabrication and characterization of RuCDzyme and TPP@RuCDzyme. (A) TEM image of the CDs. Scale bar: 2 nm (B) TEM image of the TPP@RuCDzyme. Scale bar: 100 nm. (C) Zeta data of CDs, RuCDzyme and TPP@RuCDzyme. (D) EDS mapping images of TPP@RuCDzyme. Scale bar: 100 nm. (E) XRD of the RuCDzyme and TPP@RuCDzyme. (F) FTIR of TPP, RuCDzyme and TPP@RuCDzyme. (G) XPS spectra of TPP@RuCDzyme. (H–J) XPS spectra of C (H), Ru(I) and P (J) in TPP@RuCDzyme.

respectively. The zeta potential of RuCDzyme and TPP@RuCDzyme decreased from −39.39 mV to −29.36 mV, indicating the successful conjugation of TPP on RuCDzyme. Elemental analysis revealed that Ru was homogeneously distributed within TPP@RuCDzyme, and P was homogeneously distributed on the surface of TPP@RuCDzyme (Fig. 1D). In addition, based on the X-ray diffraction pattern (Fig. 1E), TPP@RuCDzyme displayed comparable peaks to those of RuCDzyme, suggesting that the construction of TPP@RuCDzyme was successful. Moreover, the characteristic peaks of TPP and TPP@RuCDzyme observed in the Fourier transform infrared spectroscopy (Fig. 1F) were strikingly similar in nature, indicating successful modification of TPP on the RuCDzyme surface. Furthermore, the ultraviolet–visible spectra shown in Fig. S3 revealed that RuCDzyme and TPP@RuCDzyme had a similar absorption peak. Furthermore, prominent peaks in the binding energy spectra were discovered in the X-ray photoelectron spectroscopy analysis of TPP@RuCDzyme (Fig. 1G–J and S4

). This was attributed to Ru3d and P2p, suggesting the existence of the oxidised state of Ru in TPP@RuCDzyme. Figs. S5 and S6 presents the dissolution capacity of TPP@RuCDzyme in double distilled water, 0.9% NaCl solution, phosphate-buffered saline and Dulbecco's modified Eagle's medium on the first and seventh days, suggesting that TPP@RuCDzyme can be dissolved in multiple liquids and remain stable.

3.2. *Antioxidative activities of RuCDzyme and TPP@RuCDzyme*

The ROS and reactive nitrogen species (RNS) scavenging and multi-

enzyme mimetic properties of RuCDzyme and TPP@RuCDzyme were systematically evaluated. The CAT-like activity exhibited by RuCDzyme and TPP@RuCDzyme was assessed by measuring the variations in the contents of O_2 and H_2O_2 in the H_2O_2 solution. Measurements and comparative analyses of the CAT-like activity manifested by RuCDzyme and TPP@RuCDzyme were performed. Results in Fig. 2A–B and S7 demonstrate that TPP@RuCDzyme presents a remarkable level of CAT-like activity, indicating that the CAT-like activity of RuCDzyme is not influenced by TPP modification. Results in Fig. 2C reveal that the catalytic activity of TPP@RuCDzyme remains unaffected even upon the repeated addition of H_2O_2, suggesting its sustained catalytic capability.

Furthermore, owing to the highly destructive property of $O_2^{\bullet-}$, the

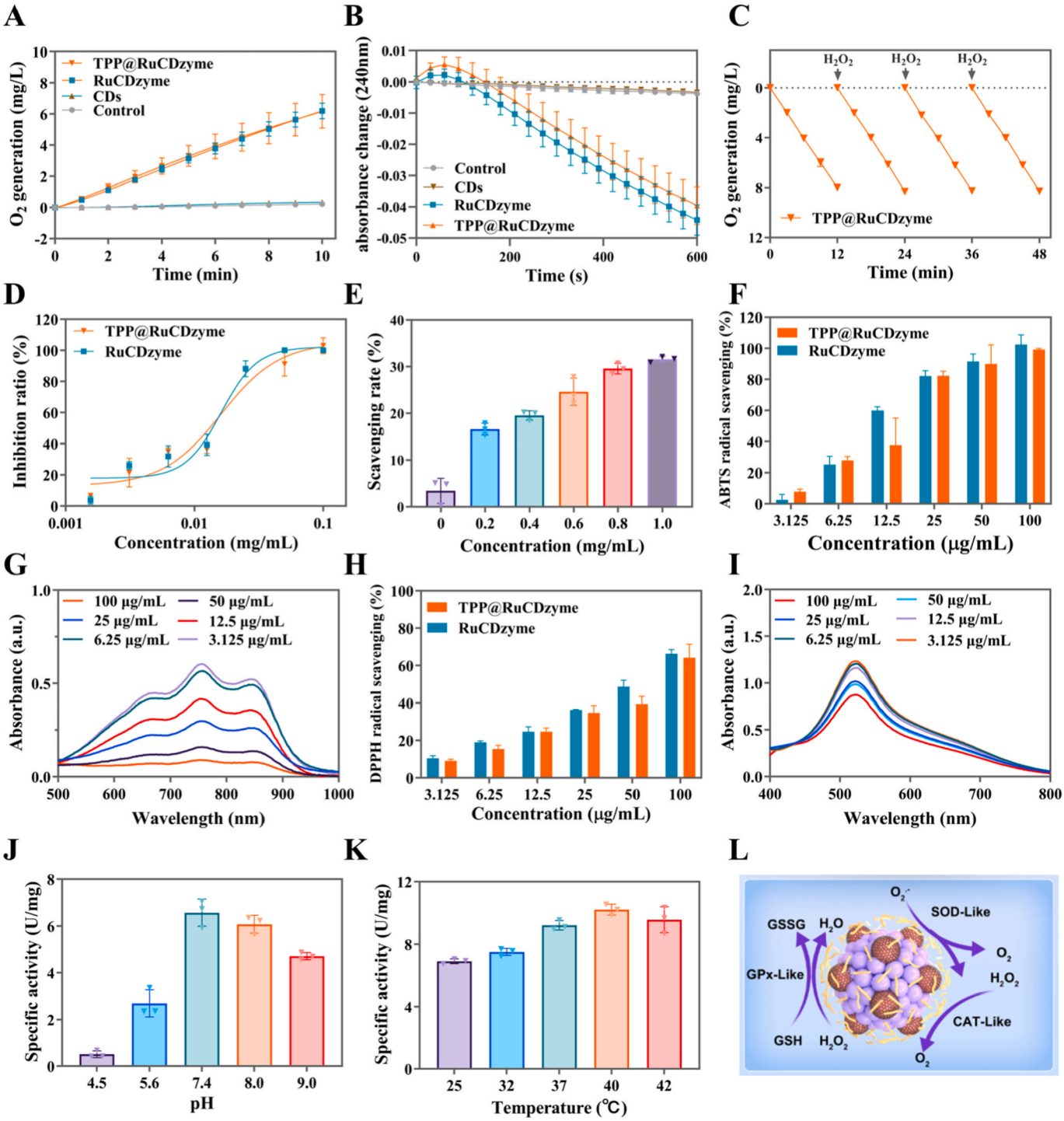

Fig. 2. Free-radical scavenging by RuCDzyme and TPP@RuCDzyme *in vitro*. (A) CAT-like activity of CDs, RuCDzyme and TPP@RuCDzyme by O_2 production over time. (B) The decomposition of H_2O_2 catalyzed by various nanozymes was monitored at 240 nm using an ultraviolet spectrophotometer. (C) Continuous H_2O_2 consumption after treatment with TPP@RuCDzyme by repetitive addition of H_2O_2. (D) SOD-like activity of RuCDzyme and TPP@RuCDzyme. (E) GPx-like activity of RuCDzyme and TPP@RuCDzyme. (F) ABTS radical scavenging ratio of RuCDzyme and TPP@RuCDzyme. (G) UV–vis absorption spectra of TPP@RuCDzyme and $ABTS^+$ after incubation with different concentration gradients. (H) DPPH radical scavenging ratio of RuCDzyme and TPP@RuCDzyme. (I) UV–vis absorption spectra of TPP@RuCDzyme and $DPPH^+$ after incubation with different concentration gradients. CAT-like activity of TPP@RuCDzyme at various pH (J) and temperature (K) conditions. (I) Schematic diagram of the multi-enzyme mimicking activity of TPP@RuCDzyme. Data represent mean ± s.d. from three independent replicates.

efficacy of RuCDzyme and TPP@RuCDzyme in terms of SOD-like activity was investigated. SOD is a crucial antioxidant enzyme for cellular defence against ROS, and its function is to transform $O_2^{\bullet-}$ into H_2O_2 and O_2. As depicted in Fig. 2D, RuCDzyme and TPP@RuCDzyme possessed relatively superior SOD-like activity. Furthermore, TPP@RuCDzyme demonstrated excellent capability in scavenging $O_2^{\bullet-}$ and $^1O_2$, as evidenced by EPR spectroscopy (Fig. S8). One possible interpretation of this outcome is that after TPP modification, the retention of the antioxidant groups in RuCDzyme remains adequate.

GPx is an endogenous anti-ROS enzyme that can effectively decompose H_2O_2 into H_2O with the assistance of GSH. Our research findings indicated that TPP@RuCDzyme exhibits some GPx-like activity at low concentrations (Fig. 2E). In summary, these results offer compelling evidence that TPP@RuCDzyme possesses multi-enzyme simulated antioxidant characteristics.

The scavenging efficacy of RuCDzyme and TPP@RuCDzyme on nitrogen-containing free radicals was determined using ABTS and DPPH radical assays. First, the free radical scavenging capacity of TPP@RuCDzyme at diverse concentrations and reaction durations was quantitatively measured using the ABTS assay. The reaction of the ABTS solution with an oxidant leads to the generation of $ABTS^+$ cationic free radicals, thereby imparting a blue–green hue. In the presence of antioxidants, the blue–green colouration is reduced, thereby resulting in a decrease in the absorption peak at approximately 734 nm. The extent of colour alteration and the corresponding reduction in absorbance are proportional to the antioxidant capacity of the test sample. After introducing TPP@RuCDzyme at various concentrations into the $ABTS^+$ environment, the intensity of the absorption peak was observed to gradually weaken with an increase in dosage, thereby significantly suppressing ABTS radical formation (Fig. 2F and G). In experiments for the investigation of RNS scavenging, DPPH free radicals are typically employed as a model. It possesses a prominent absorption peak at a wavelength of 517 nm, which declines in the presence of antioxidants. Consistent with the results of the ABTS assay, when TPP@RuCDzyme was introduced into the $DPPH^+$ solution at different concentrations, a progressive reduction in the intensity of the absorption peak was observed as the dosage increased. This indicates that TPP@RuCDzyme effectively scavenged DPPH free radicals in a dose-dependent manner (Fig. 2H and I).

Natural enzymes have certain limitations and are prone to being influenced by temperature, pH and metal ions, subsequently losing their catalytic activity or even having their structures compromised. In contrast, nanozymes typically possess excellent catalytic activity under various temperatures and pH values. As depicted in Fig. 2J and K, TPP@RuCDzyme not only demonstrated optimal functionality within a broader pH range but also exhibited thermal stability. These results substantiate that TPP@RuCDzyme possesses relatively high multi-enzyme-mimetic antioxidant activity and stability (Fig. 2L).

3.3. *RuCDzyme- and TPP@RuCDzyme-mediated protection of H_2O_2-stimulated cells*

During AKI, renal tubules within the kidney tissue are more prone to the influence of oxidative stress. Consequently, in the early phase of AKI, safeguarding renal tubules from ROS-induced damage can notably mitigate renal functional disorders. Hence, the human kidney 2 (HK-2) cell line was used to examine the cytoprotective effects of TPP@RuCDzyme against ROS damage *in vitro*. First, 2-(2-methoxy-4-nitrophenyl)-3-(4-nitrophenyl)-5-(2,4-disulfophenyl)-2H-tetrazolium, monosodium salt (CCK-8) was employed to assess the cytotoxicity of TPP@RuCDzyme. The results of the CCK-8 assay indicated that when TPP@RuCDzyme was co-incubated with HK-2 cells, AC16 cells and LX-2 cells for 24 and 48 h, three types of cells cytotoxicity were insignificant when the TPP@RuCDzyme concentration was <100 μg/mL (Fig. 3A–S9 and S10). In addition, the results of the haemolysis experiment (Fig. S11) indicated that when the TPP@RuCDzyme concentration was <400 μg/mL, the haemolysis rate remained <4.5 %, suggesting that TPP@RuCDzyme possesses excellent biocompatibility. The results of the haemolysis experiment were in accordance with previous studies, suggesting that TPP@RuCDzyme generally exhibits low toxicity at relatively low concentrations.

Excessive oxidative stress (such as prolonged exposure to H_2O_2) can induce cell death. To assess the impact of TPP@RuCDzyme on H_2O_2-induced cell viability, a series of treatments were performed on HK-2 cells. H_2O_2 cytotoxicity to HK-2 cells was preliminarily evaluated using the fluorescence double staining method [calcein-AM/propidium iodide (PI)]. H_2O_2 at a dose of 400 μM effectively killed a considerable proportion of HK-2 cells, which could be reflected by cells stained red with the PI dye (Fig. S12), as confirmed by the CCK-8 assay (Fig. 3B). These treatments included RuCDzyme and TPP@RuCDzyme. After these treatments, cells were exposed to H_2O_2 (400 μM), and cell viability was evaluated using the CCK-8 assay. As depicted in Fig. 3C, the cell viability of the TPP@RuCDzyme-treated group was superior to that of the RuCDzyme-treated group. The same results were obtained using the fluorescent dual staining method (calcein-AM/PI). The fluorescence images and semi-quantitative analysis derived from the calcein-AM/PI staining experiment also demonstrated that the therapeutic effect of the TPP@RuCDzyme treatment group was superior to that of the RuCDzyme treatment group (Fig. 3D and E). Subsequently, the DCFH-DA fluorescent dye was employed to quantitatively determine intracellular ROS levels in HK-2 cells. As depicted in Fig. 3F–H, the ROS levels in cells pre-incubated with RuCDzyme and TPP@RuCDzyme were lower than those in cells treated with H_2O_2 alone, and the ROS level in the TPP@RuCDzyme-treated group was even lower. The quantitative results of flow cytometry also demonstrated the same outcome. Moreover, the Annexin V/PI apoptosis assay (Fig. 3I and J) was employed to assess the impact of TPP@RuCDzyme and/or H_2O_2 (400 μM) on HK-2 cell death. The average percentage of apoptotic cells in the control group was 4.96%, whereas that in the H_2O_2 single-treatment group was 21.19%. The proportion of apoptotic cells in the TPP@RuCDzyme treatment group was 5.95%, whereas that in the RuCDzyme treatment group was 9.44%. All outcomes demonstrated that RuCDzyme and TPP@RuCDzyme could suppress H_2O_2-induced cell apoptosis, with TPP@RuCDzyme showing a more pronounced inhibitory action.

Mitochondria are the energy metabolic center of cells and the primary targets of numerous pathogenic factors. The main functions of the mitochondria are to supply energy to cells and regulate cell signal transduction, cell death and biosynthetic metabolism. Under normal conditions, the mitochondria can maintain a homeostatic balance through their oxidative and antioxidant systems, eliminating excessive ROS. When imbalance occurs in the homeostasis of the oxidative and antioxidant systems in an organism, the mitochondrial electron respiratory chain is impaired, resulting in the generation of a large amount of ROS. Consequently, eliminating ROS within the mitochondria is important for maintaining mitochondrial function and cell viability. To assess the influences of RuCDzyme and TPP@RuCDzyme on mitochondrial function, the JC-1 fluorescent probe was used to monitor the alterations in the mitochondrial membrane potential (MMP). Under normal circumstances, JC-1 accumulates abundantly within the mitochondrial matrix, generating intense red fluorescence. Nevertheless, when exposed to H_2O_2, the MMP drops and causes intense green fluorescence. The results obtained from fluorescence microscopy and flow cytometry are depicted in Fig. 4A–C. In H_2O_2-induced injury, there was a decline in the MMP, presenting intense green fluorescence. The RuCDzyme and TPP@RuCDzyme treatment groups displayed a certain extent of recovery of the MMP. The TPP@RuCDzyme treatment group restored the MMP to a level comparable to that of the control group. Furthermore, the Mitosox Red fluorescent probe was employed to assess the ROS levels within the mitochondria in the different treatment groups (Fig. 4D). Once the mitochondria were induced by H_2O_2, a distinct red fluorescent signal was imparted. In contrast, the mitochondrial ROS levels in the RuCDzyme and TPP@RuCDzyme treatment groups were

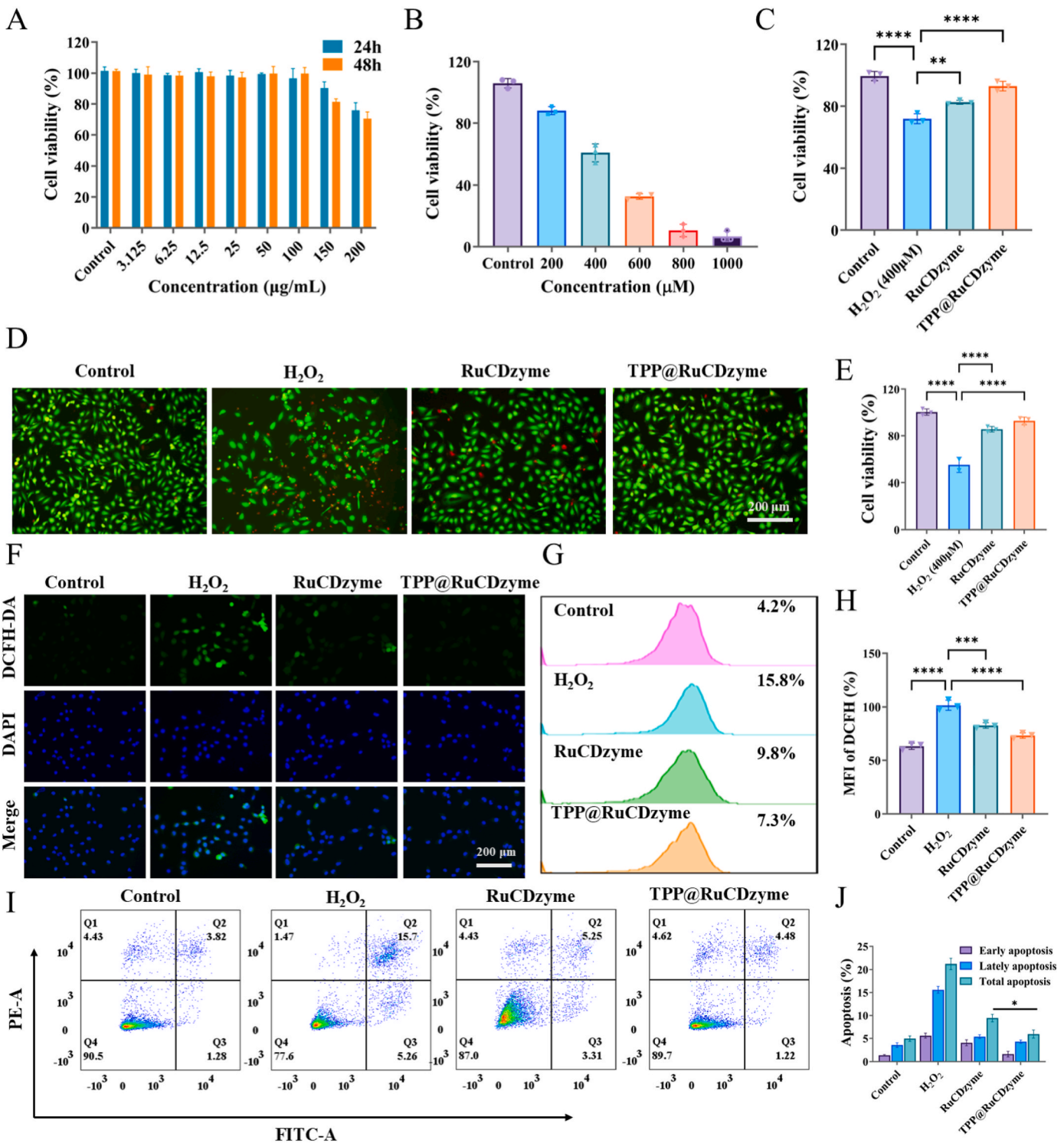

Fig. 3. RuCDzyme and TPP@RuCDzyme mediated protection of H_2O_2-stimulated cells. (A) Cell viability of HK-2 cells treated with various concentrations of TPP@RuCDzyme for 24 and 48 h as determined by CCK8 assay (n = 3). (B) Viability of HK-2 cells treated with varying doses of H_2O_2 (n = 3). (C) Cell viability of HK-2 cells under H_2O_2 with/without same concentrations of RuCDzyme and TPP@RuCDzyme (n = 3). (D) Fluorescence images and (E) semi-quantitative results of injured HK-2 cells stained with AM/PI after various treatments. Scale bar: 200 μm. (F) Confocal fluorescence images of DFCH-DA stained HK-2 cells after different treatments. Scale bar: 200 μm. (G) Flow cytometry analysis and (H) quantification of DFCH-DA stained HK-2 cells after different treatments. (I) Flow cytometry results of apoptotic cells in HK-2 cells under different treatment conditions. (J) Statistical analysis of apoptotic cell ratios in HK-2 cells under different treatment conditions. (ns: non-significant, $^*P < 0.05$, $^{**}P < 0.01$, $^{***}P < 0.001$, $^{****}P < 0.0001$).

substantially decreased. To explore the co-localisation capacity of TPP@RuCDzyme, a co-localisation experiment on MitoTracker (green)-labeled HK-2 cells was performed under a fluorescence microscope. In Fig. 4E and S13, in contrast to RuCDzyme, TPP@RuCDzyme demonstrated a targeting effect on mitochondria within different time periods.

Subsequently, the relevant indices were assessed to determine the restoration of mitochondrial function. First, the intracellular ATP levels

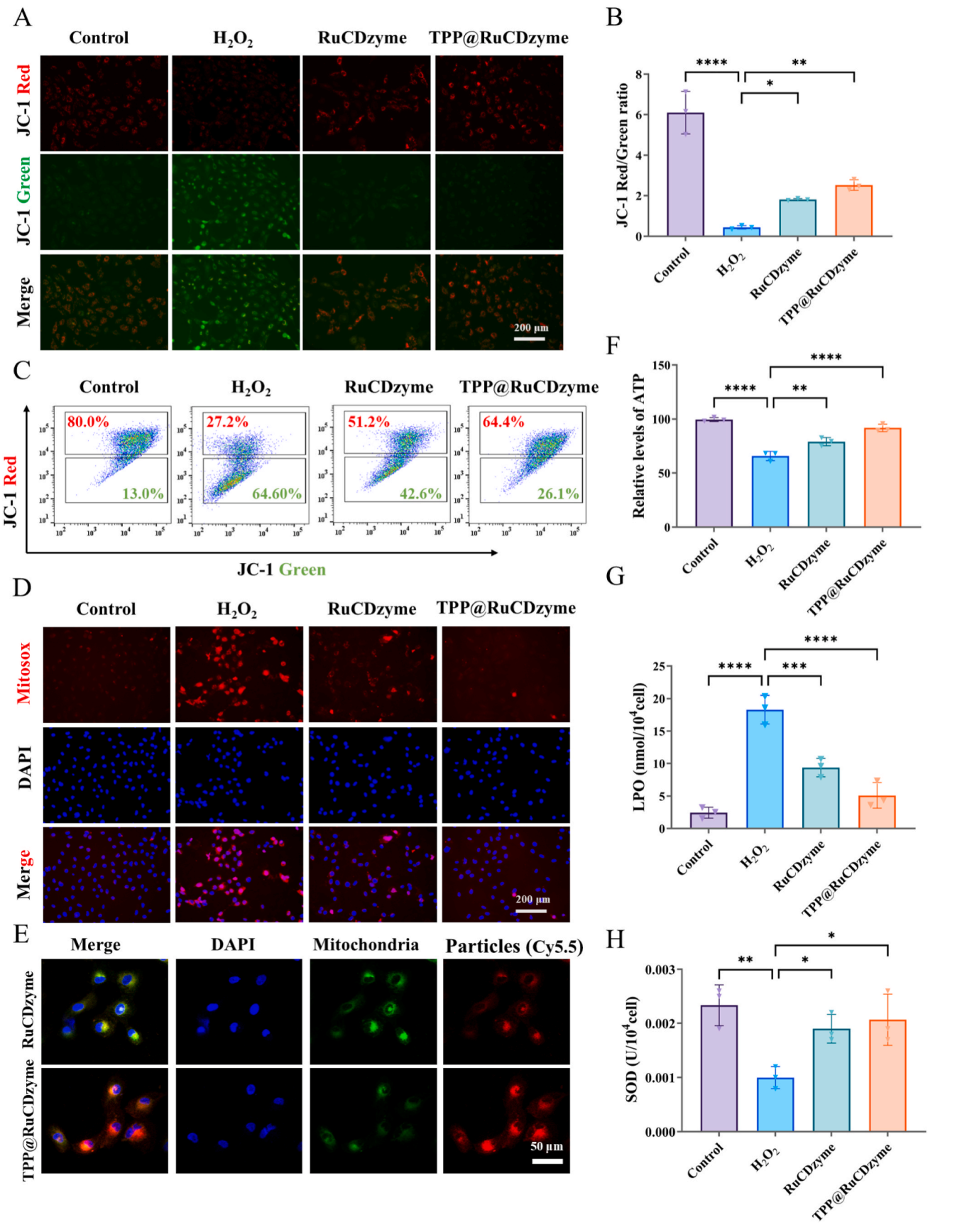

(caption on next page)

Fig. 4. TPP@RuCDzyme regulates mitochondrial function against H_2O_2-induced apoptosis. (A) Representative images of JC-1 fluorescence staining are analyzed by confocal microscopy. Scale bar: 200 μm. (B) The ratio of JC-1 aggregates (red)/JC-1 monomer (green) fluorescence was analyzed based on confocal picture results to assess mitochondrial membrane potential. (C) Flow cytometry quantification of JC-1 stained HK-2 cells after different treatments. (D) Representative images show the mitochondrial ROS levels of HK-2 cells after co incubation with different treatment groups for 24 h, monitored using Mitosox fluorescent probes. Scale bar: 200 μm. (E) The representative image shows the co-localisation of Cy5.5 labeled nanoparticles and Mito Tracker Green labeled mitochondria in HK-2 cells (incubated for 2 h). Scale bar: 200 μm. The expression levels of ATP (F), LPO (G), and SOD (H) in HK-2 cells of different treatment groups (n = 3). (ns: non-significant, $^{*}P < 0.05$, $^{**}P < 0.01$, $^{***}P < 0.001$, $^{****}P < 0.0001$). (For interpretation of the references to colour in this figure legend, the reader is referred to the Web version of this article.)

in different treatment groups, which directly indicate the mitochondrial energy supply, were evaluated. The oxidative stress induced by H_2O_2 significantly reduced the ATP levels, whereas the TPP@RuCDzyme treatment group exhibited superior ATP recovery ability compared with the RuCDzyme treatment group, highlighting the significance of targeting mitochondria for restoring mitochondrial function (Fig. 4F). Lipid peroxidation (LPO) is the product of the reaction between oxygen free radicals and polyunsaturated fatty acids. Under normal circumstances, the LPO content is extremely low. Nevertheless, under the oxidative stress induced by H_2O_2, the LPO reaction intensifies and the level of LPO increases. Notably, treatment with RuCDzyme and TPP@RuCDzyme significantly decreased the LPO level (Fig. 4G). SOD plays a vital role in catalysing ROS, safeguarding the mitochondria from oxidative damage and maintaining mitochondrial function. Hence, the SOD levels in different experimental groups were evaluated after treatment. As depicted in Fig. 4H, upon exposure of HK-2 cells to H_2O_2, the SOD level significantly decreased, but the RuCDzyme and TPP@RuCDzyme treatment groups restored the SOD level to varying degrees. These results suggested that TPP@RuCDzyme targeting the mitochondria can effectively eliminate ROS and modulate mitochondrial function.

3.4. *In vivo* therapeutic efficacy of RuCDzyme and TPP@RuCDzyme in AKI mice

Subsequently, a study was conducted to explore the *in vivo* therapeutic efficacy of TPP@RuCDzyme on AKI, considering its remarkable capacity for eliminating ROS and favourable biosafety. The experimental procedure involved inducing rhabdomyolysis-induced AKI in normal mice through intramuscular injection of a 50% glycerol solution (Fig. 5A). The weight gain of TPP@RuCDzyme-treated AKI mice was similar to that of healthy mice, whereas AKI mice showed a sharp decrease in weight within 24 h (Fig. 5B). Furthermore, the levels of two crucial renal function indicators, CRE and BUN, in the serum of the TPP@RuCDzyme-treated AKI mice were significantly lower than those in the serum of AKI mice (Fig. 5C and D). No significant disparity in the CRE and BUN levels was observed between healthy and TPP@RuCDzyme-treated AKI mice, confirming that TPP@RuCDzyme treatment for glycerol-induced AKI has favourable efficacy. Furthermore, hematoxylin and eosin staining were performed on renal tissues to obtain conclusive evidence for AKI treatment with TPP@RuCDzyme. Casts are substances that form within renal tubules due to the denaturation of proteins and are commonly used as a diagnostic indicator for kidney disorders. Fig. 5E and F depict the injury conditions in the kidney sections of AKI mice. Notably, AKI mice treated with TPP@RuCDzyme exhibited fewer damaged structures than AKI mice treated with RuCDzyme. Subsequently, terminal deoxynucleotidyl transferase-mediated dUTP nick end labelling (TUNEL) was employed to identify apoptotic cells in the kidney tissue sections. The fluorescence images and quantitative analysis (Fig. 5G and H) revealed a considerable accumulation of apoptotic cells in the AKI group compared with that in the control group. Nevertheless, the percentage of apoptotic cells in the TPP@RuCDzyme treatment group was relatively lower than that in the RuCDzyme treatment group, suggesting that TPP@RuCDzyme possesses superior anti-apoptotic effects *in vivo*.

To investigate the effects of TPP@RuCDzyme more comprehensively *in vivo*, frozen kidney tissues were stained with DHE. In Fig. 6A, the inhibition of ROS generation in AKI mice by TPP@RuCDzyme treatment was most obvious compared with that in the RuCDzyme and AKI groups. Furthermore, the SOD level was measured in the renal tissues. As mentioned earlier, SOD is a crucial protease responsible for eliminating ROS within renal cells *in vivo*. The SOD level in the TPP@RuCDzyme-treated AKI mice was comparable to that in normal mice, whereas a significant reduction in the SOD level was observed in AKI mice (Fig. 6B). Furthermore, the levels of kidney injury molecule-1 (Kim-1) and haem oxygenase-1 (HO-1), both regarded as important biomarkers of kidney injury, were assessed in renal tissues. In the AKI mouse model, the Kim-1 and HO-1 levels in the renal tissues of the TPP@RuCDzyme-treated group were comparable to those in the renal tissues of healthy mice (Fig. 6C and D), whereas treating AKI mice with RuCDzyme led to a partial reduction in the Kim-1 and HO-1 levels. In addition, this study investigated the potential inhibitory effect of TPP@RuCDzyme on DNA damage. The level of 8-hydroxy-2′-deoxyguanosine (8-OHdG) in the kidneys of mice treated with TPP@RuCDzyme was significantly lower than that in the kidneys of AKI mice (Fig. 6E). The decrease in 8-OHdG can be used as an indicator of oxidative stress and a criterion for determining DNA damage. We further evaluated the expression of SOD2 in mouse kidneys through immunofluorescence experiments. As shown in Fig. 6F and G, the SOD2 levels in TPP@RuCDzyme-treated AKI mice were comparable to those in normal mice, while a significant decrease in SOD levels was observed in untreated AKI mice.

As stated previously, Kim-1 is a type I membrane glycoprotein that is typically undetectable in healthy kidneys but increases in the damaged proximal tubular regions of AKI mice. As depicted in Fig. 7A and B, Kim-1 expression was the most prominent in AKI mice, with the fluorescence intensity increasing nearly 14-fold compared with that in the normal group, indicating severe tubular cell injury. In addition, in the TPP@RuCDzyme and RuCDzyme treatment groups, the relative fluorescence intensities of Kim-1 decreased by approximately 80 % and 70 %, respectively, indicating that TPP@RuCDzyme can rapidly deplete ROS at the lesion site, thereby mitigating tubular cell injury. Subsequently, Masson staining was performed on the kidney tissues of different treatment groups. As presented in Fig. 7C, after treatment with TPP@RuCDzyme, the muscle fibres in the kidney tissues were conspicuously reduced, suggesting that TPP@RuCDzyme can prevent the occurrence of renal fibrosis in AKI mice. We then further analyzed the time-dependent changes in renal concentration of TPP@RuCDzyme and RuCDzyme. Distinct red fluorescence was observed in kidneys at 0.5 h post-injection, with fluorescence intensity progressively increasing over time, reaching peak levels at approximately 12h before gradual decline due to drug excretion (Fig. 7D and S14). Notably, TPP@RuCDzyme@Cy5.5 exhibited significantly higher peak fluorescence intensity (12 h) and prolonged fluorescence persistence (24h) in kidneys compared to RuCDzyme@Cy5.5 (Fig. 7E).

3.5. *In vivo* toxicity assessment

Next, the influence of TPP@RuCDzyme (20 mg/kg) on the blood chemistry, inflammatory cytokine levels and histopathology of major organ tissues in healthy mice was assessed to uncover its *in vivo* biocompatibility. As depicted in Figs. 8A and 14 days after the intravenous injection of TPP@RuCDzyme, no necrosis, congestion or haemorrhage was detected in the heart, liver, spleen and lungs. No significant inflammatory lesions or tissue damage were noted in the glomeruli, tubules, collecting ducts and urethra (Fig. 8B). Continuous

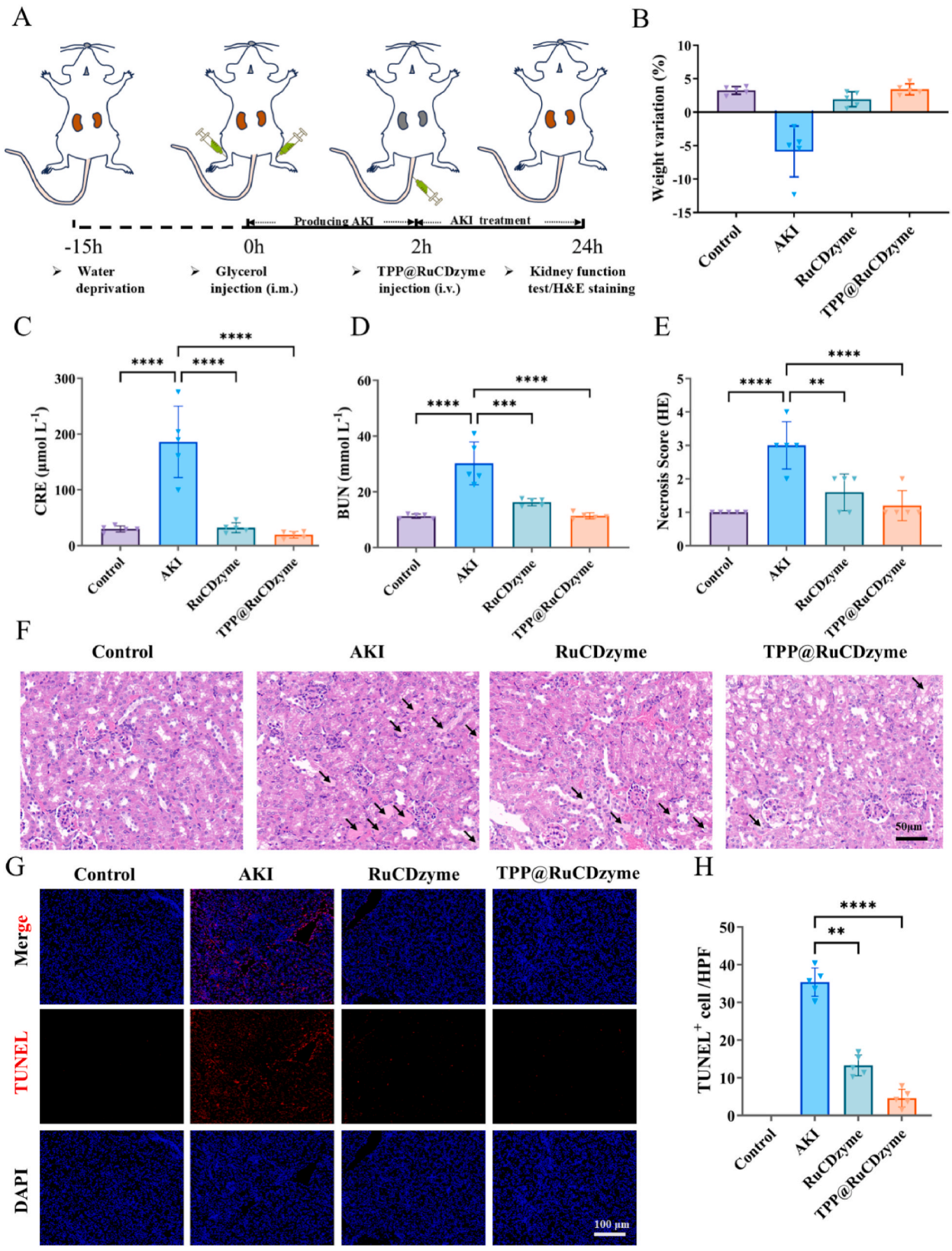

Fig. 5. Therapeutic efficiency of TPP@RuCDzyme on AKI mice. (A) Schematic Diagram of Establishment and Treatment Plan for AKI Mice. (B) Body Weight Changes of AKI Mice after different treatments at 24 h. (C and D) The levels of CRE and BUN in AKI mice after different treatments at 24 h. (E) Scoring of renal tubular injury in mice after different treatments. (F) H&E staining of renal tissue in each treatment group. Scale bar: 200 μm. (G) The level of apoptosis in kidneys labeled by TUNEL assay (red fluorescence). Scale bar: 200 μm. (H) Quantification of the percentage of TUNEL^{+} apoptotic cells. HPF, High power field. Data represent mean ± s.d. from five independent replicates (ns: non-significant, $^{*}P < 0.05$, $^{**}P < 0.01$, $^{***}P < 0.001$, $^{****}P < 0.0001$). (For interpretation of the references to colour in this figure legend, the reader is referred to the Web version of this article.)

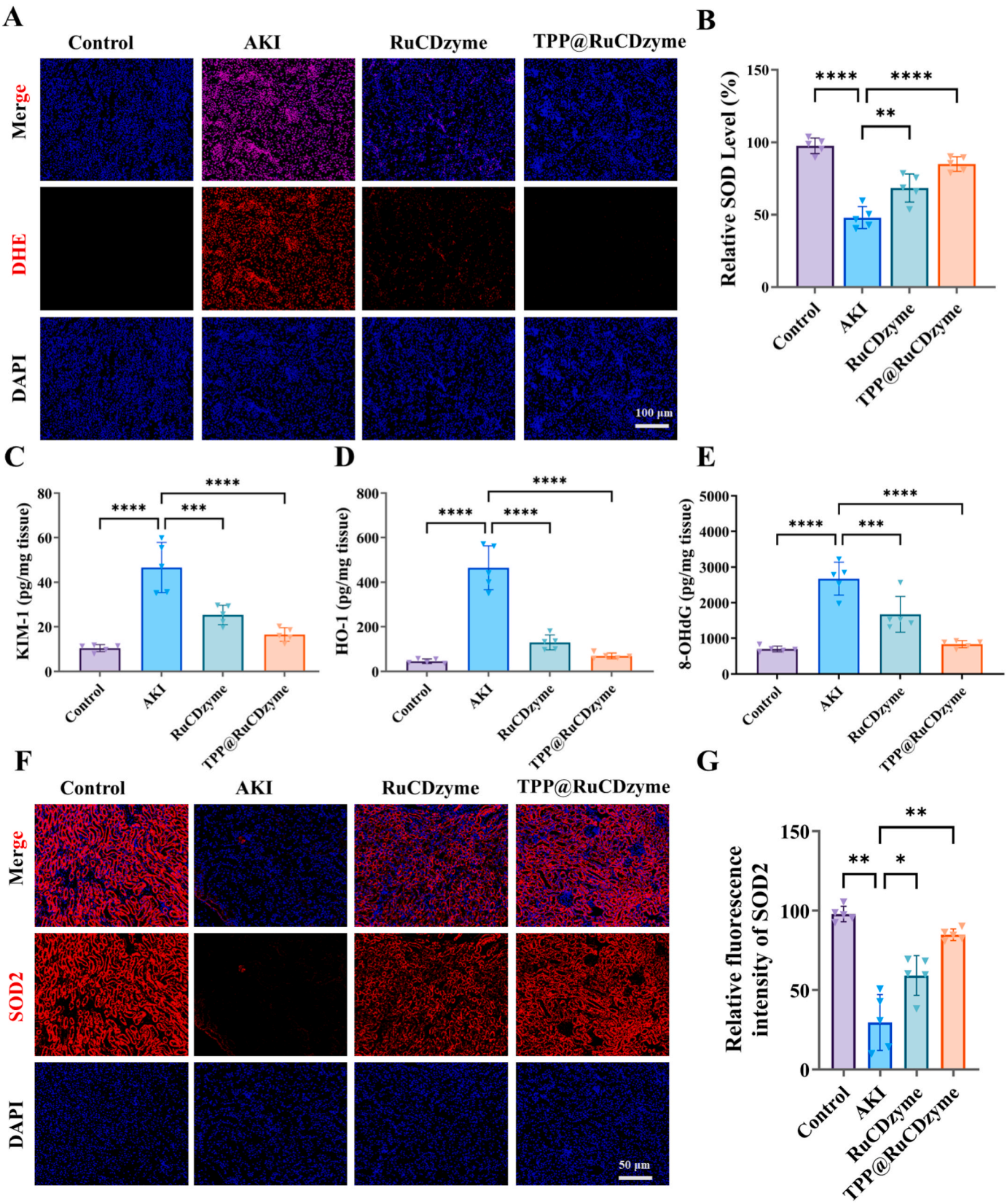

Fig. 6. Analysis of renal tissue after TPP@RuCDzyme treatment. (A) Representative images of dihydroethidine (DHE) and DAPI staining in renal tissue from different treatment groups. Scale bar: 100 μm. (B–E) The expression levels of SOD, Kim-1, HO-1, and 8-OHdG in the renal tissue homogenates of different treatment groups. (F) Representative fluorescence images of SOD2 in kidney tissues from different treatment groups. Scale bar: 50 μm. (G) Quantitative analysis of relative fluorescence intensity of SOD2 in different treatment groups. Data represent mean ± s.d. from five independent replicates (ns: non-significant, $^{*}P < 0.05$, $^{**}P < 0.01$, $^{***}P < 0.001$, $^{****}P < 0.0001$).

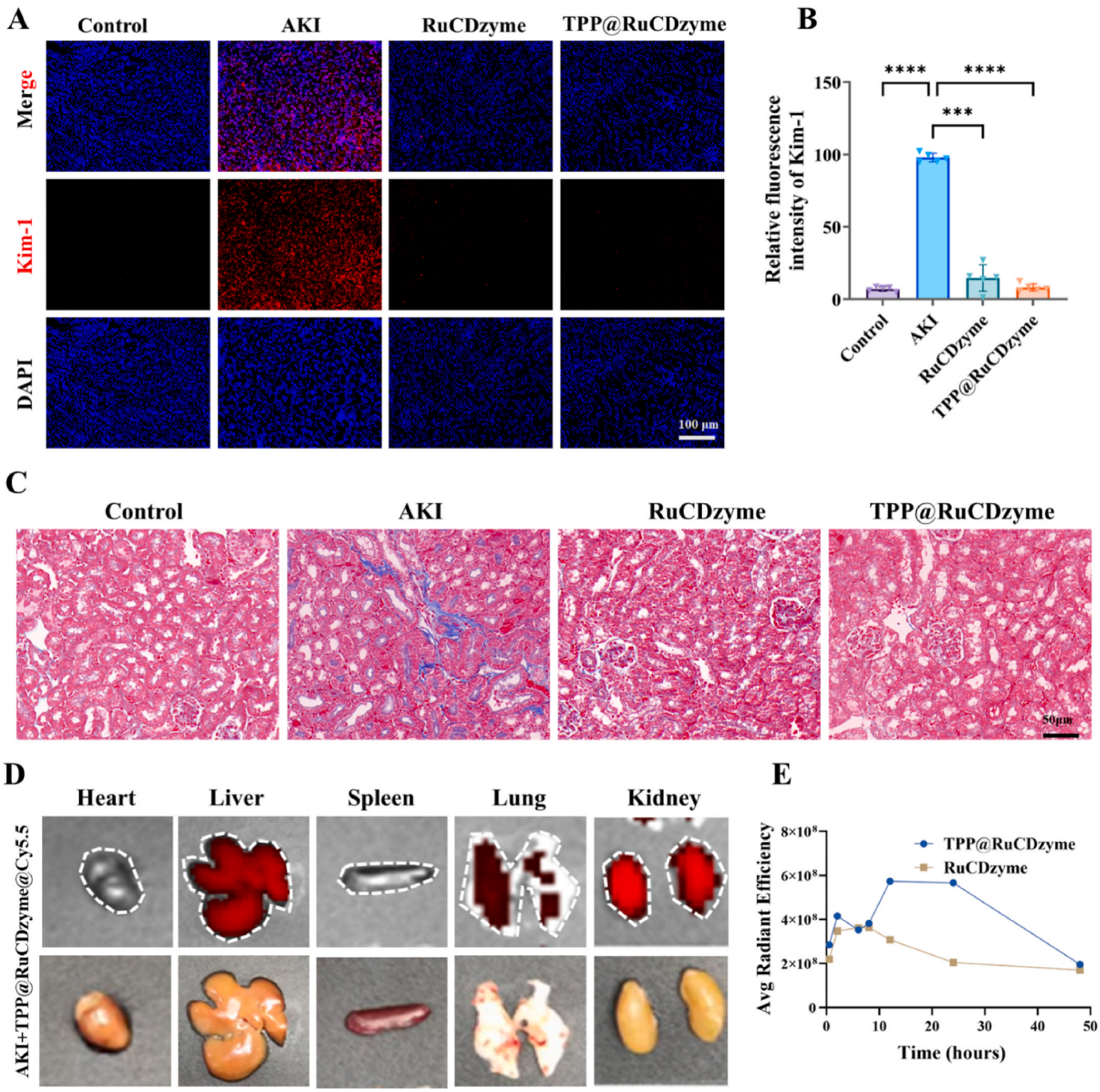

Fig. 7. Therapeutic efficiency of TPP@RuCDzyme on AKI mice and biological distribution of TPP@RuCDzyme in mouse kidneys. (A) Representative images of immunostaining of Kim-1 in different treatment groups. Scale bar: 100 μm. (B) Quantitative analysis of immunostaining for Kim-1 in different treatment groups. (C) Representative images of Masson staining for renal injury in different treatment groups. Scale bar: 50 μm. (D) Representative fluorescence images of different organs in AKI mice 12 h after intravenous injection of TPP@RuCDzyme@Cy5.5. (E) The fluorescence intensity in kidneys after drug injection (0.5–48 h) from different groups. Data represent mean ± s.d. from five independent replicates (ns: non-significant, $*P < 0.05$, $**P < 0.01$, $***P < 0.001$, $****P < 0.0001$).

monitoring of changes in body weight revealed no significant differences in body weight between the control and TPP@RuCDzyme treatment groups (Fig. 8C). Meanwhile, blood biochemical indicators, including CRE, BUN, alanine aminotransferase (ALT) and aspartate aminotransferase (AST), were examined, which indicated normal liver and kidney functions (Fig. 8D and E). In addition, the results of the complete blood analysis (Fig. 8F–J) indicated that there was no significant difference in haematology between the TPP@RuCDzyme treatment and control groups. All experimental results unanimously demonstrated that TPP@RuCDzyme exhibits negligible toxicity in organisms, possesses good biocompatibility and holds therapeutic advantages in AKI treatment.

4. Conclusions

A novel anti-oxidation nanozyme (RuCDzyme) has been effectively synthesized through the conjugation of CDs synthesized via the hydrothermal method with ruthenium element. Subsequently, the TPP moiety was introduced onto RuCDzyme, resulting in the construction of TPP@RuCDzyme with enhanced mitochondrial targeting capability.

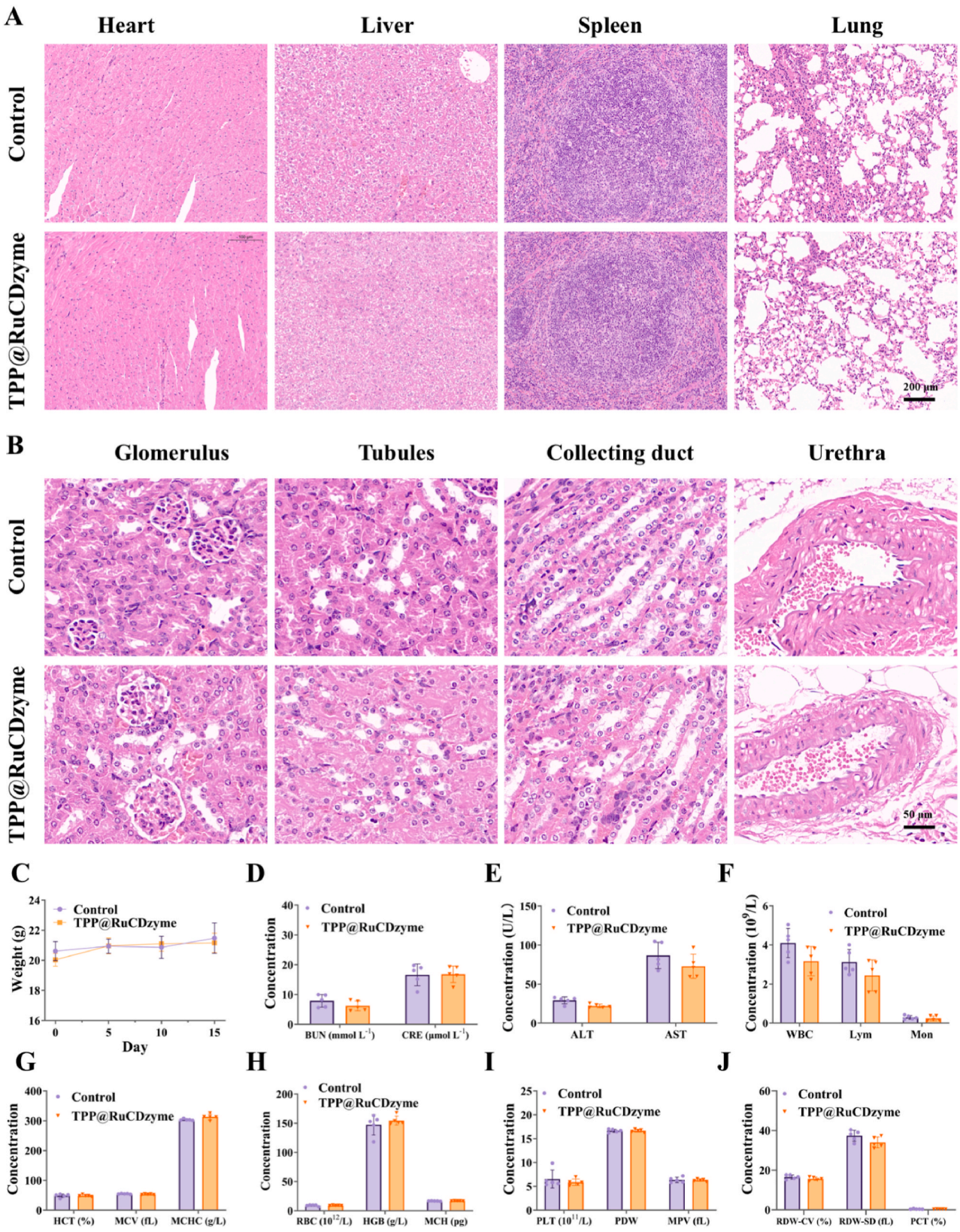

Fig. 8. In vivo toxicity assessment of TPP@RuCDzyme. (A) In vivo toxicity evaluation of TPP@RuCDzyme on major organs (heart, liver, spleen, lung) after subcutaneous administration for 14 days. Scale bar: 200 μm. (B) In vivo toxicity assessment of TPP@RuCDzyme on kidneys after subcutaneous administration for 14 days. Scale bar: 50 μm. (C) Weight changes after intravenous injection of TPP@RuCDzyme or PBS. (D) The renal function indicators CRE and BUN of normal mice and mice injected with TPP@RuCDzyme. (E) The liver function indicators alanine transaminase (ALT) and aspartate transaminase (AST) of normal mice and mice injected with TPP@RuCDzyme. (F–J) Serum biochemical assays and serological data of normal mice and mice after injection with TPP@RuCDzyme. Data represent mean ± s.d. from five independent replicates.

TPP@RuCDzyme exhibits multiple enzymatic activities, including CAT-, SOD-and GPx-like activity. These activities can effectively eliminate various ROS, such as H_2O_2 and $O_2^{\bullet-}$. The protective effect of TPP@RuCDzyme on H_2O_2-induced HK-2 cells is attributed to its good biocompatibility and excellent antioxidant performance. TPP@RuCDzyme exhibits no renal toxicity both *in vitro* and *in vivo*, and possesses excellent mitochondrial repair and cell apoptosis prevention abilities, thus inhibiting renal injury and restoring renal function. In summary, TPP@RuCDzyme as a nano-antioxidant shows significant potential in alleviating AKI induced by rhabdomyolysis.

CRediT authorship contribution statement

Jiangpeng Pan: Writing – original draft, Visualization, Validation, Supervision, Resources, Methodology, Investigation, Formal analysis, Data curation. **Juntao Wang:** Software, Resources, Project administration, Investigation, Funding acquisition, Formal analysis, Data curation. **Wei Wang:** Data curation, Investigation, Resources, Software, Supervision, Validation, Visualization. **Ziyang Liu:** Project administration, Methodology, Investigation, Formal analysis, Data curation. **Shuai Huo:** Resources, Methodology, Investigation, Formal analysis, Data curation. **Lei Yan:** Methodology, Investigation, Funding acquisition, Data curation. **Wei Jiang:** Writing – review & editing, Writing – original draft, Visualization, Validation, Supervision, Software, Resources, Methodology, Investigation, Formal analysis, Data curation, Conceptualization. **Fengmin Shao:** Visualization, Validation, Supervision, Software, Resources, Project administration, Investigation, Funding acquisition, Formal analysis, Data curation. **Yue Gu:** Visualization, Validation, Supervision, Software, Resources, Project administration, Methodology, Investigation, Funding acquisition, Formal analysis, Data curation, Conceptualization.

Declaration of competing interest

We declare that we have no financial and personal relationships with other people or organizations that can inappropriately influence our work, there is no professional or other personal interest of any nature or kind in any product, service and/or company that could be construed as influencing the position presented in, or the review of, the manuscript entitled, “Renal-clearable and Mitochondria-targeted Carbon Dot Nanozymes for Acute Kidney Injury Alleviation”.

Acknowledgements

J. Pan., and J. Wang contributed equally to this work. This work was supported by the funding of Zhongyuan Scholars of Henan Provincial Health Commission (224000510005), Zhongyuan Scholar Workstation (234400510024), Technology Attack Plan Project of Henan Province (242102311062), and Medical Science and Technology Attack Plan Project of Henan Province (SBGJ202302002).

Appendix A. Supplementary data

Supplementary data to this article can be found online at https://doi.org/10.1016/j.mtbio.2025.101717.

Data availability

Data will be made available on request.

References

[1] P. Pickkers, M. Darmon, E. Hoste, M. Joannidis, M. Legrand, M. Ostermann, J. R. Prowle, A. Schneider, M. Schetz, Acute kidney injury in the critically ill: an updated review on pathophysiology and management, Intensive Care Med. 47 (8) (2021) 835–850, https://doi.org/10.1007/s00134-021-06454-7.

[2] M.T. James, M. Bhatt, N. Pannu, M. Tonelli, Long-term outcomes of acute kidney injury and strategies for improved care, Nat. Rev. Nephrol. 16 (4) (2020) 193–205, https://doi.org/10.1038/s41581-019-0247-z.

[3] J.A. Kellum, P. Romagnani, G. Ashuntantang, C. Ronco, A. Zarbock, H.J. Anders, Acute kidney injury, Nat. Rev. Dis. Primers 7 (1) (2021) 52, https://doi.org/10.1038/s41572-021-00284-z.

[4] C. Ronco, R. Bellomo, J.A. Kellum, Acute kidney injury, Lancet 394 (10212) (2019) 1949–1964, https://doi.org/10.1016/s0140-6736(19)32563-2.

[5] B.A. Naved, J.V. Bonventre, J.A. Hubbell, N.A. Hukriede, B.D. Humphreys, C. Kesselman, M.T. Valerius, A.P. McMahon, S.J. Shankland, J.A. Wertheim, M.J. V. White, M.P. de Caestecker, I.A. Drummond, Kidney repair and regeneration: perspectives of the NIDDK (Re)Building a Kidney consortium, Kidney Int. 101 (5) (2022) 845–853, https://doi.org/10.1016/j.kint.2022.02.023.

[6] P.I. Good, L. Li, H.A. Hurst, I. Serrano Herrera, K. Xu, M. Rao, D.A. Bateman, Q. Al-Awqati, V.D. D'Agati, F. Costantini, F. Lin, Low nephron endowment increases susceptibility to renal stress and chronic kidney disease, JCI Insight 8 (3) (2023), https://doi.org/10.1172/jci.insight.161316.

[7] D. Ni, D. Jiang, C.J. Kutyreff, J. Lai, Y. Yan, T.E. Barnhart, B. Yu, H.J. Im, L. Kang, S.Y. Cho, Z. Liu, P. Huang, J.W. Engle, W. Cai, Molybdenum-based nanoclusters act as antioxidants and ameliorate acute kidney injury in mice, Nat. Commun. 9 (1) (2018) 5421, https://doi.org/10.1038/s41467-018-07890-8.

[8] Q. Weng, H. Sun, C. Fang, F. Xia, H. Liao, J. Lee, J. Wang, A. Xie, J. Ren, X. Guo, F. Li, B. Yang, D. Ling, Catalytic activity tunable ceria nanoparticles prevent chemotherapy-induced acute kidney injury without interference with chemotherapeutics, Nat. Commun. 12 (1) (2021) 1436, https://doi.org/10.1038/s41467-021-21714-2.

[9] R. Yan, W. Cui, W. Ma, J. Li, Z. Liu, Y. Lin, Typhaneoside-tetrahedral framework nucleic acids system: mitochondrial recovery and antioxidation for acute kidney injury treatment, ACS Nano 17 (9) (2023) 8767–8781, https://doi.org/10.1021/acsnano.3c02102.

[10] L. Su, J. Zhang, H. Gomez, J.A. Kellum, Z. Peng, Mitochondria ROS and mitophagy in acute kidney injury, Autophagy 19 (2) (2023) 401–414, https://doi.org/10.1080/15548627.2022.2084862.

[11] Q. Huang, Y. Yang, T. Zhao, Q. Chen, M. Liu, S. Ji, Y. Zhu, Y. Yang, J. Zhang, H. Zhao, Y. Nan, K. Ai, Passively-targeted mitochondrial tungsten-based nanodots for efficient acute kidney injury treatment, Bioact. Mater. 21 (2023) 381–393, https://doi.org/10.1016/j.bioactmat.2022.08.022.

[12] M. Zhao, Y. Wang, L. Li, S. Liu, C. Wang, Y. Yuan, G. Yang, Y. Chen, J. Cheng, Y. Lu, J. Liu, Mitochondrial ROS promote mitochondrial dysfunction and inflammation in ischemic acute kidney injury by disrupting TFAM-mediated mtDNA maintenance, Theranostics 11 (4) (2021) 1845–1863, https://doi.org/10.7150/thno.50905.

[13] R. Duan, Y. Li, R. Zhang, X. Hu, Y. Wang, J. Zeng, M. Gao, Reversing acute kidney injury through coordinated interplay of anti-inflammation and iron supplementation, Adv. Mater. 35 (28) (2023) e2301283, https://doi.org/10.1002/adma.202301283.

[14] D.A.C. Messerer, R. Halbgebauer, B. Nilsson, H. Pavenstädt, P. Radermacher, M. Huber-Lang, Immunopathophysiology of trauma-related acute kidney injury, Nat. Rev. Nephrol. 17 (2) (2021) 91–111, https://doi.org/10.1038/s41581-020-00344-9.

[15] P. Bhargava, R.G. Schnellmann, Mitochondrial energetics in the kidney, Nat. Rev. Nephrol. 13 (10) (2017) 629–646, https://doi.org/10.1038/nrneph.2017.107.

[16] H. Scholz, F.J. Boivin, K.M. Schmidt-Ott, S. Bachmann, K.U. Eckardt, U.I. Scholl, P. B. Persson, Kidney physiology and susceptibility to acute kidney injury: implications for renoprotection, Nat. Rev. Nephrol. 17 (5) (2021) 335–349, https://doi.org/10.1038/s41581-021-00394-7.

[17] Q. Chen, Y. Nan, Y. Yang, Z. Xiao, M. Liu, J. Huang, Y. Xiang, X. Long, T. Zhao, X. Wang, Q. Huang, K. Ai, Nanodrugs alleviate acute kidney injury: manipulate RONS at kidney, Bioact. Mater. 22 (2023) 141–167, https://doi.org/10.1016/j.bioactmat.2022.09.021.

[18] A. Sureshbabu, S.W. Ryter, M.E. Choi, Oxidative stress and autophagy: crucial modulators of kidney injury, Redox Biol. 4 (2015) 208–214, https://doi.org/10.1016/j.redox.2015.01.001.

[19] R. Zhang, L. Cheng, Z. Dong, L. Hou, S. Zhang, Z. Meng, O. Betzer, Y. Wang, R. Popovtzer, Z. Liu, Ultra-small natural product based coordination polymer nanodots for acute kidney injury relief, Mater. Horiz. 8 (4) (2021) 1314–1322, https://doi.org/10.1039/d0mh00193g.

[20] J. Gu, P. Zhang, H. Li, Y. Wang, Y. Huang, L. Fan, X. Ma, X. Qian, J. Xi, Cerium-luteolin nanocomplexes in managing inflammation-related diseases by antioxidant and immunoregulation, ACS Nano 18 (8) (2024) 6229–6242, https://doi.org/10.1021/acsnano.3c09528.

[21] X. Zhang, L. Liang, F. Wang, P.A. Jose, K. Chen, C. Zeng, Irisin-encapsulated mitochondria-targeted biomimetic nanotherapeutics for alleviating acute kidney injury, Adv. Sci. 11 (38) (2024) e2402805, https://doi.org/10.1002/advs.202402805.

[22] Y. Nie, L. Wang, S. Liu, C. Dai, T. Cui, Y. Lei, X. You, X. Wang, J. Wu, Z. Zheng, Natural ursolic acid based self-therapeutic polymer as nanocarrier to deliver natural resveratrol for natural therapy of acute kidney injury, J. Nanobiotechnol. 21 (1) (2023) 484, https://doi.org/10.1186/s12951-023-02254-x.

[23] A. Robert, B. Meunier, How to define a nanozyme, ACS Nano 16 (5) (2022) 6956–6959, https://doi.org/10.1021/acsnano.2c02966.

[24] H. Wang, K. Wan, X. Shi, Recent advances in nanozyme research, Adv. Mater. 31 (45) (2019) e1805368, https://doi.org/10.1002/adma.201805368.

[25] Y.G. Kim, Y. Lee, N. Lee, M. Soh, D. Kim, T. Hyeon, Ceria-based therapeutic antioxidants for biomedical applications, Adv. Mater. 36 (10) (2024) e2210819, https://doi.org/10.1002/adma.202210819.

[26] C.J. Neal, E. Kolanthai, F. Wei, M. Coathup, S. Seal, Surface chemistry of biologically active reducible oxide nanozymes, Adv. Mater. 36 (10) (2024) e2211261, https://doi.org/10.1002/adma.202211261.
[27] M.S. Lord, J.F. Berret, S. Singh, A. Vinu, A.S. Karakoti, Redox active cerium oxide nanoparticles: current status and burning issues, Small 17 (51) (2021) e2102342, https://doi.org/10.1002/smll.202102342.
[28] D. Xu, L. Wu, H. Yao, L. Zhao, Catalase-like nanozymes: classification, catalytic mechanisms, and their applications, Small 18 (37) (2022) e2203400, https://doi.org/10.1002/smll.202203400.
[29] J. Xiang, X. Yang, M. Tan, J. Guo, Y. Ye, J. Deng, Z. Huang, H. Wang, W. Su, J. Cheng, L. Zheng, S. Liu, J. Zhong, J. Zhao, NIR-enhanced Pt single atom/g-C(3)N (4) nanozymes as SOD/CAT mimics to rescue ATP energy crisis by regulating oxidative phosphorylation pathway for delaying osteoarthritis progression, Bioact. Mater. 36 (2024) 1–13, https://doi.org/10.1016/j.bioactmat.2024.02.018.
[30] W. Wang, J. Duan, W. Ma, B. Xia, F. Liu, Y. Kong, B. Li, H. Zhao, L. Wang, K. Li, Y. Li, X. Lu, Z. Feng, Y. Sang, G. Li, H. Xue, J. Qiu, H. Liu, Trimanganese tetroxide nanozyme protects cartilage against degeneration by reducing oxidative stress in osteoarthritis, Adv. Sci. 10 (17) (2023) e2205859, https://doi.org/10.1002/advs.202205859.
[31] S. Ge, A. Sun, X. Zhou, P. Niu, Y. Chen, X. Bao, M. Yu, Z. Zhong, J. Sun, G. Li, Functionalized nanozyme microcapsules targeting deafness prevention via mitochondrial homeostasis remodeling, Adv. Mater. (2024) e2413371, https://doi.org/10.1002/adma.202413371.
[32] Z. Wang, Y. Zhao, Y. Hou, G. Tang, R. Zhang, Y. Yang, X. Yan, K. Fan, A thrombin-activated peptide-templated nanozyme for remedying ischemic stroke via thrombolytic and neuroprotective actions, Adv. Mater. 36 (10) (2024) e2210144, https://doi.org/10.1002/adma.202210144.
[33] H. Zhao, H. Zhao, M. Li, Y. Tang, X. Xiao, Y. Cai, F. He, H. Huang, Y. Zhang, J. Li, Twin defect-rich Pt ultrathin nanowire nanozymes alleviate inflammatory skin diseases by scavenging reactive oxygen species, Redox Biol. 70 (2024) 103055, https://doi.org/10.1016/j.redox.2024.103055.
[34] H. Ding, F. Du, P. Liu, Z. Chen, J. Shen, DNA-carbon dots function as fluorescent vehicles for drug delivery, ACS Appl. Mater. Interfaces 7 (12) (2015) 6889–6897, https://doi.org/10.1021/acsami.5b00628.
[35] A. Nair, J.T. Haponiuk, S. Thomas, S. Gopi, Natural carbon-based quantum dots and their applications in drug delivery: a review, Biomed. Pharmacother. 132 (2020) 110834, https://doi.org/10.1016/j.biopha.2020.110834.
[36] M.X. Zhang, Y.L. Liang, Y.A. Zhang, L.M. Zhang, N. Wang, Y. Zhou, Y.F. Wang, M. L. Cui, Z.X. Yu, M.Z. Zhang, Y.N. Ma, Oral carbon dot nanozymes with red fluorescence and superoxide dismutase-like activity for colitis bioimaging and inflammation management, Chem. Eng. J. 493 (2024), https://doi.org/10.1016/j.cej.2024.152842.
[37] T.C. Wareing, P. Gentile, A.N. Phan, Biomass-based carbon dots: current development and future perspectives, ACS Nano 15 (10) (2021) 15471–15501, https://doi.org/10.1021/acsnano.1c03886.
[38] M. Yang, H. Li, X. Liu, L. Huang, B. Zhang, K. Liu, W. Xie, J. Cui, D. Li, L. Lu, H. Sun, B. Yang, Fe-doped carbon dots: a novel biocompatible nanoplatform for multi-level cancer therapy, J. Nanobiotechnol. 21 (1) (2023) 431, https://doi.org/10.1186/s12951-023-02194-6.
[39] K.K. Chan, S.H.K. Yap, K.T. Yong, Biogreen synthesis of carbon dots for Biotechnology and nanomedicine applications, Nano-Micro Lett. 10 (4) (2018) 72, https://doi.org/10.1007/s40820-018-0223-3.
[40] J. Wang, Y. Fu, Z. Gu, H. Pan, P. Zhou, Q. Gan, Y. Yuan, C. Liu, Multifunctional carbon dots for biomedical applications: diagnosis, therapy, and theranostic, Small 20 (3) (2024) e2303773, https://doi.org/10.1002/smll.202303773.
[41] R. Gui, H. Jin, Z. Wang, J. Li, Black phosphorus quantum dots: synthesis, properties, functionalized modification and applications, Chem. Soc. Rev. 47 (17) (2018) 6795–6823, https://doi.org/10.1039/c8cs00387d.
[42] W. Lu, Y. Guo, J. Zhang, Y. Yue, L. Fan, F. Li, C. Dong, S. Shuang, A high catalytic activity nanozyme based on cobalt-doped carbon dots for biosensor and anticancer cell effect, ACS Appl. Mater. Interfaces 14 (51) (2022) 57206–57214, https://doi.org/10.1021/acsami.2c19495.
[43] Y.J. Zhang, W.H. Gao, Y.A. Ma, L.L. Cheng, L. Zhang, Q.G. Liu, J.Y. Chen, Y. R. Zhao, K.S. Tu, M.Z. Zhang, C. Liu, Integrating Pt nanoparticles with carbon nanodots to achieve robust cascade superoxide dismutase-catalase nanozyme for antioxidant therapy, Nano Today 49 (2023), https://doi.org/10.1016/j.nantod.2023.101768.
[44] C. Liu, W.B. Fan, W.X. Cheng, Y.P. Gu, Y.M. Chen, W.H. Zhou, X.F. Yu, M.H. Chen, M.R. Zhu, K.L. Fan, Q.Y. Luo, Red emissive carbon dot superoxide dismutase nanozyme for bioimaging and ameliorating acute lung injury, Adv. Funct. Mater. 33 (19) (2023), https://doi.org/10.1002/adfm.202213856.
[45] Z. Liu, L. Xie, K. Qiu, X. Liao, T.W. Rees, Z. Zhao, L. Ji, H. Chao, An ultrasmall RuO (2) nanozyme exhibiting multienzyme-like activity for the prevention of acute kidney injury, ACS Appl. Mater. Interfaces 12 (28) (2020) 31205–31216, https://doi.org/10.1021/acsami.0c07886.
[46] C. Wu, X. Han, W. Feng, Z. Liu, L. Chen, B. Zhou, Y. Chen, J. Shi, Multi-enzymatic activities of ultrasmall ruthenium oxide for anti-inflammation and neuroprotection, Chem. Eng. J. 411 (2021) 128543, https://doi.org/10.1016/j.cej.2021.128543.